Petroleum Science 23 (2026) 2030–2045

Contents lists available at ScienceDirect

Petroleum Science

journal homepage: www.keaipublishing.com/en/journals/petroleum-science

Original Paper

Pore structure-controlled CO_2 huff-n-puff efficiency in Jimusar shale oil reservoirs: Insights from classified oil reservoirs

Qing Li [a,b], Ying-Yan Li [c], Pei-Yu Li [a], Ji-Xiang He [c], Yi-Lei Song [a,d], Chi-Yang Yu [c], Zhao-Jie Song [a,*], Hao-Chen Ren [a]

[a] State Key Laboratory of Petroleum Resources and Engineering, China University of Petroleum (Beijing), Beijing, 102249, China
[b] Xinjiang Oilfield Company, PetroChina, Karamay, 834000, Xinjiang, China
[c] Exploration and Development Research Institution, PetroChina Xinjiang Oilfield Company, Karamay, 834000, Xinjiang, China
[d] School of Petroleum, China University of Petroleum (Beijing) at Karamay, Karamay, 834000, Xinjiang, China

ARTICLE INFO

Article history:
Received 13 June 2025
Received in revised form
20 December 2025
Accepted 21 December 2025
Available online 24 December 2025

Edited by Yan-Hua Sun

Keywords:
Shale oil reservoirs
Pore structures
CO_2 huff-n-puff
Nuclear magnetic resonance
Productive pore threshold

ABSTRACT

CO_2 huff-n-puff is a promising enhanced oil recovery technique for shale oil reservoirs, but its efficiency in relation to pore structure across classified oil reservoirs remains unclear. This study investigates three reservoir classes (Types I–III) in the Jimusar Sag using high pressure mercury intrusion, nitrogen adsorption, and NMR to characterize pore architectures. Results show that the shale cores from the Jimusar shale oil reservoir are overall dominated by medium pores, with generally small pore radii. Among them, the Type I oil reservoir class has a higher proportion of large pores (> 300 nm), whereas the Type III oil reservoir class has a higher proportion of small pores (< 50 nm) than the other two classes. Online NMR monitored CO_2 huff-n-puff experiments under reservoir conditions (363.15 K, injection pressure > 24 MPa) reveal significant cumulative oil recovery differences: 56.36% (Type I), 46.81% (Type II), and 28.30% (Type III) after four cycles. Recovery correlates with pore size: The Type I oil reservoir class, with a higher proportion of large pores, exhibits stronger CO_2 flow capacity, whereas the Type III oil reservoir class, with a larger proportion of small pores, significantly restricts oil mobilization. A second derivative analysis of the recovery–pore radius curve quantifies mobilization thresholds, indicating a lower limit effective pore radius of 20–35 nm. Sensitivity analysis shows that increasing injection pressure more effectively improves recovery and lowers the mobilization threshold than extending soaking time.

1. Introduction

In recent years, unconventional oil and gas reservoirs have become a hotspot in global petroleum exploration and development. Particularly, shale oil reservoirs have garnered significant attention and are gradually becoming a key focus for future exploration and development (Li et al., 2025; Lv et al., 2025; Song et al., 2025a, 2025b; Wang et al., 2025). Among them, the Permian Lucaogou Formation shale oil reservoir in the Jimusar Sag of northwest China has surpassed a cumulative production of one million tons after over ten years of development (Xie et al., 2022). Nevertheless, the exploitation of the Jimusar shale oil reservoir still faces numerous challenges, such as reservoir spaces characterized by micron-sized pores and nanometer scale throats, complex pore throat structures, and significant variations in pore size distribution and structural characteristics among different reservoir types (He et al., 2025; Pang et al., 2022; Y. Song et al., 2024b; Z. Song et al., 2024; Zhu et al., 2025). Furthermore, current production faces rapid decline rates, low production, and low oil recovery, highlighting an urgent need for technologies capable of effectively enhancing oil recovery (Xie et al., 2022). Consequently, to substantially enhance the development effectiveness of Jimusar shale oil, research on enhanced oil recovery (EOR) technologies is imperative.

Among numerous methods for enhancing oil recovery, CO_2 huff-n-puff has demonstrated high sweep efficiency, with both

* Corresponding author.
E-mail address: songz@cup.edu.cn (Z.-J. Song).
Peer review under the responsibility of China University of Petroleum (Beijing).

https://doi.org/10.1016/j.petsci.2025.12.033

laboratory experiments and field tests confirming its capability to significantly improve shale oil recovery (Li et al., 2019a). In the Jimusar field test, a CO_2 huff-n-puff pilot in J30 well recovered approximately 1.9% of the original oil in place after a single cycle, underscoring the strong potential of CO_2 EOR in the Lucaogou Formation (Shi et al., 2024). The effectiveness of this technology is closely related to the reservoir's pore structure, which fundamentally controls fluid storage and transport mechanisms. Current approaches for characterizing pore structures can be broadly categorized into three groups: direct imaging, fluid invasion experiments, and indirect non-destructive techniques (Clarkson et al., 2012; Zhou et al., 2024).

Direct imaging methods, such as scanning electron microscopy (SEM) and focused ion beam scanning electron microscopy (FIB-SEM), enable high resolution visualization of pore networks (L. Chen et al., 2022; Kelly et al., 2016; Wang et al., 2016; Wang and Sun, 2021). For example, Y. Zhang et al. (2023) applied FIB-SEM to analyze pore systems in lacustrine shale samples, while Meng et al. (2024) combined it with super resolution algorithms to reconstruct 3D pore models and evaluate their impact on fluid flow. Fluid invasion methods, including mercury intrusion porosimetry (MIP) and gas adsorption, interpret pore structures by monitoring fluid behavior during injection. Ge et al. (2016) proposed a fractal model based on high pressure MIP data to estimate permeability, and Xiao et al. (2020) developed an integrated approach for full scale pore throat distribution characterization in tight reservoirs. Pan et al. (2022) employed MIP among other methods to study factors influencing pore structure and oil mobility. In contrast, indirect methods such as nuclear magnetic resonance (NMR) provide quantitative, non-destructive analysis of pore size distribution and fluid occupancy (Wang and Wang, 2022; Yao et al., 2010; P. Zhang et al., 2023). NMR is especially valuable when combined with MIP and nitrogen adsorption, as it allows for the calibration of transverse relaxation time (T_2) to pore throat radius, enabling a comprehensive characterization across multiple pore scales.

Numerous laboratory and numerical studies have investigated the mechanisms of CO_2 huff-n-puff in shale oil reservoirs (He et al., 2024; Li et al., 2024). Experimental work by Li et al. (2019b) highlighted the importance of oil swelling and viscosity reduction, while molecular dynamics simulations by Tan et al. (2024) revealed how CO_2 extracts lighter hydrocarbons from mineral surfaces, which aligns with the findings of Hartono et al. (2024). Y. Han et al. (2024) developed a diffusion model under fracture network conditions, showing that molecular diffusion enhances CO_2 penetration in low permeability matrices. Y. Song et al. (2024a) developed a numerical model to study how nano-confinement and the composition of oil influenced enhanced shale oil recovery via CO_2 huff-n-puff. Wang et al. (2024) proposed a fully coupled numerical model that combines multiple mechanisms to evaluate production performance during CO_2 EOR in shale reservoirs. Despite these advances, there remains a relative lack of research examining the pore scale dynamics of oil mobilization during CO_2 huff-n-puff.

A powerful tool for addressing this problem is the online NMR technique, which integrates low field NMR with core flooding experiments. This method allows continuous, non-invasive monitoring of fluid distribution throughout the EOR process (Y. Chen et al., 2022; Gong et al., 2022; Song and Kausik, 2019). Previous studies have used NMR to track asphaltene depositions during CO_2 huff-n-puff (Shen and Sheng, 2017). Song et al. (2022) conducted N_2 huff-n-puff experiments using NMR techniques to study crude oil recovery in reservoirs with varying pore structures. Gao et al. (2024) created an experimental approach built upon the online NMR analysis method to investigate pore scale mobilization characteristics of CO_2 huff-n-puff in shale reservoirs. X. Han et al. (2024) proposed the CO_2-water-alternating-gas (WAG) huff-n-puff technique for shale reservoirs and systematically investigated the fluid flow characteristics of oil, gas, and water during the injection, soaking, and production stages under NMR monitoring.

Although CO_2 injections have been widely acknowledged for their effectiveness in enhancing recovery in shale oil, the lower limits of oil mobilization pore radii by CO_2 remain insufficiently studied. Therefore, this research utilizes an integrated approach combining high pressure mercury intrusion, nitrogen adsorption, and NMR techniques to systematically study the pore throat structures of different reservoir types in the Jimusar shale oil reservoir. Subsequently, an online NMR analysis system was established to conduct CO_2 huff-n-puff experiments, recording the NMR T_2 spectra under reservoir conditions, observing fluid distribution changes, and discussing the lower limits of oil mobilization pore radii by CO_2 and the feasibility of enhancing oil recovery across different reservoir types. Besides, this study examines the enhanced oil recovery performance of CO_2 huff-n-puff across different pore sizes at different parameters, for example soaking times and injection pressures.

2. Experimental

2.1. Materials

Natural cores from the Jimusar shale oil reservoir in the Xinjiang Oilfield formed the basis of the experimental samples in this work, as shown in Fig. 1. Their basic properties are summarized in Table 1. The Jimusar shale is a mixed shale. Its lithologies are dominated by dolomitic silt rich mudstone, dolomite bearing argillaceous siltstone, argillaceous siltstone, dolomitic siltstone, and calcareous argillaceous siltstone. The mineral assemblage is chiefly feldspar, dolomite, quartz, and lithic fragments, with a low clay content (Z. Song et al., 2024). As shown in Fig. 2, the three core samples have relatively high contents of feldspar and dolomite. Fig. 3 indicates that core #1 features a pore type assemblage dominated by residual intergranular pores and intergranular dissolution pores, with a lithology of dolomitic sandstone; core #2 is characterized mainly by intergranular and intragranular dissolution pores, with a lithology of dolomitic fine siltstone; and core #3 is dominated by intragranular dissolution pores with minor intergranular dissolution pores, with a lithology of argillaceous fine siltstone. In terms of lithology and mineralogy, all three

Fig. 1. Experimental core samples from Jimusar shale oil reservoir.

Table 1
Physical properties of experimental core samples.

Core No.	Length, cm	Diameter, cm	Weight, g	Porosity, %	Permeability, 10^{-3} μm^2
#1	4.44	2.50	50.96	12.11	0.17274
#2	4.88	2.52	57.19	7.98	0.06198
#3	5.15	2.51	60.78	5.86	0.00462

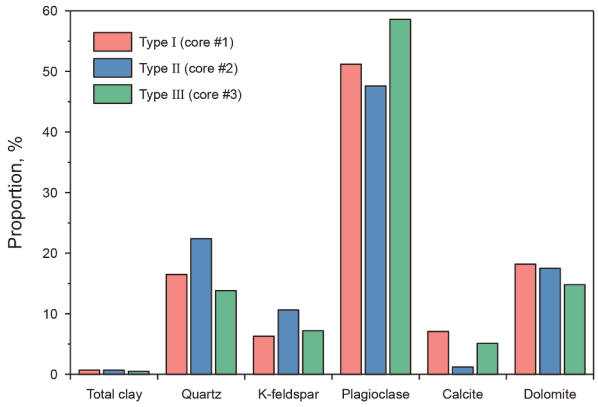

Fig. 2. Mineral composition of the three core samples.

samples exhibit the typical characteristics of the Jimusar shale, while their petrophysical properties differ markedly, allowing them to represent distinct reservoir types for subsequent investigations. Based on petrophysical characteristics, core #1 is classified as a Type I oil reservoir class, core #2 as Type II, and core #3 as Type III. The crude oil for the experiments was taken from the same block after dehydration and degassing; its four-component composition is given in Table 2. Measured by gas chromatography, the crude oil composition is shown in Table 3. The sample is dominated by the C_{15}–C_{28} fractions. Under reservoir conditions (46.53 MPa and 366.15 K), this oil has a viscosity of 9.25 mPa·s. The CO_2 used in the flooding tests has a purity of 99.99%. Heat-shrink tubing, which was chosen for its high-temperature resistance, corrosion resistance, and ability to prevent CO_2 escape, was employed to seal and encase the cores during testing.

2.2. Apparatus

We employed high pressure mercury intrusion and N_2 adsorption methods to characterize the pore size distribution in the shale cores. The mercury intrusion measurements were performed on a Micromeritics AutoPore IV 9520 fully automated porosimeter (Micromeritics, USA). Nitrogen adsorption analysis was carried out using a BK300C surface area and pore size analyzer (JWGB Instruments), employing the manufacturer's specialized rock sample tubes. These tubes accommodate intact rock samples up to 25 mm in diameter and 0–110 mm in length, eliminating the need for sample grinding and thus preserving the original pore structure.

For the CO_2 huff-n-puff testing and analysis, the experimental apparatus consists of three major subsystems: (1) the displacement system (including the injection, temperature-control, and pressure-control modules), (2) the online NMR monitoring system, and (3) the data acquisition system. The displacement system comprises ISCO high-pressure, high-precision syringe pumps and intermediate containers; intermediate containers store crude oil and CO_2, each of which is delivered into the core holder via the ISCO pumps. The online NMR monitoring system includes a MacroMR12-060H-1 NMR instrument (MacroMR, Suzhou) and a non-magnetic, high-temperature/high-pressure core holder. The NMR instrument at a magnetic field strength of 0.3±0.05 T (12 MHz resonance frequency) and accommodates samples with diameters of 25–150 mm. The data acquisition system consists of a back-pressure valve, a signal-acquisition computer, and a gas–liquid separator; the back-pressure valve regulates outlet pressure, the separator removes liberated gas, and the computer records NMR T_2 spectra and other real-time data. A schematic of the apparatus and testing procedure is shown in Fig. 4.

2.3. Procedures

Two primary experimental methodologies were utilized in this work: (1) characterization of the pore-structure features of shale core samples, and (2) CO_2 huff-n-puff testing and analysis.

2.3.1. High pressure mercury intrusion experiment

Mercury intrusion porosimetry (MIP) is well suited for characterizing macropores in shale because it offers a fixed configuration instrument, rapid measurement, minimal requirements on sample shape or size, and high measurement pressures. The main experimental procedure is as follows:

Core samples (1 cm^3) were oven-dried, placed in the penetrometer, and subjected to low- and high-pressure mercury injections to obtain intrusion extrusion curves over a pressure range of 0.001–300 MPa. The resulting data were used to derive macropore size distributions and pore connectivity.

2.3.2. Nitrogen adsorption experiment

Because nitrogen adsorption experiments exhibit high sensitivity to micropore and mesopore distributions and can effectively characterize nano-scale pore structures at low temperatures, thereby complementing the limitations of high-pressure mercury intrusion, this study employs nitrogen adsorption as a key method to finely resolve small-pore throat features. The main steps are as follows:

Samples were washed, dried (333.15 K, 24 h), and degassed (423.15 K, 6 h) before testing. Adsorption desorption measurement was performed at relative pressures (P/P_0) of 0.01–0.99 (All measurements were conducted at a constant temperature of 77 K to ensure the accuracy of pore size distribution characterization.). The density functional theory (DFT) method was applied for surface area analysis, and pore size distributions were derived from desorption data.

2.3.3. Pore size distribution test on formation water saturated samples

Pore size distribution is measured by NMR on rock samples fully saturated with formation water; pore sizes and distributions are inferred from relaxation characteristics (e.g., the T_2 relaxation time distribution). This method rapidly and non-destructively acquires pore structure information under conditions closely resembling subsurface fluids, thus more accurately reflecting true reservoir pore characteristics. The main steps are as follows:

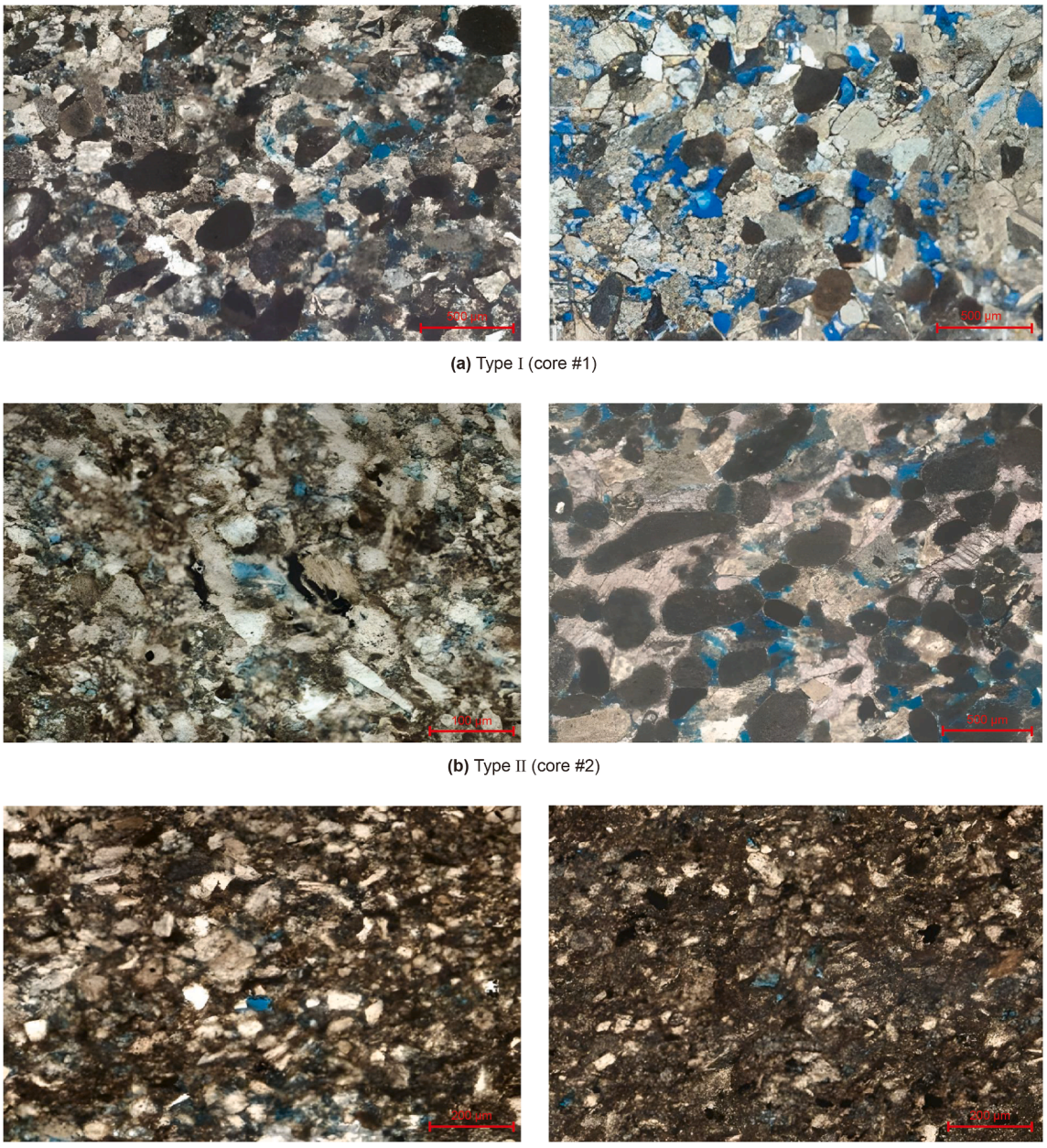

Fig. 3. Micrographs showing casting thin sections of typical lithologies in the Permian Lucaogou Formation, Jimusar Sag, Junggar Basin.

Table 2
Four-component composition of the crude oil used.

Saturates, %	Aromatics, %	Resins, %	Asphaltenes, %
49.85	16.29	24.13	9.73

(1) Core drying and baseline NMR: The core sample was oven-dried, and its dry mass was recorded. The baseline NMR signal of the dry rock was acquired to obtain the dry state T_2 spectrum.
(2) Formation water saturation: Samples were evacuated under vacuum for 24 h and then were saturated with synthetic brine at 363.15 K and 20 MPa for 7 d (25,000 ppm total dissolved solids; NaCl: $CaCl_2$: $MgCl_2{\cdot}6H_2O$ = 7:0.6:0.4, mass ratio). The saturated mass was recorded.
(3) Saturated state NMR acquisition: Using optimized NMR measurement parameters, the T_2 relaxation time spectrum of the water saturated core was acquired.
(4) Data processing: The measured transverse relaxation times (T_2) of the pore fluids were converted into a pore size distribution curve.

2.3.4. CO_2 huff-n-puff experiment

In the CO_2 huff-n-puff experiments on different reservoir types, an online NMR system was used to monitor fluid signals within the core in real time. This allowed determination of the lower limits of oil mobilization pore radii by CO_2 under different gas injection parameters (injection pressures and soaking times) and quantitative assessment of recovery from pores of different scales.

Table 3
Compositions of the crude oil.

Component	Content, wt%	Component	Content, wt%	Component	Content, wt%
C_1	0	C_{11}	1.774	C_{24}	5.048
C_2	0	C_{12}	1.910	C_{25}	5.530
C_3	0.026	C_{13}	3.542	C_{26}	3.837
i-C_4	0.026	C_{14}	2.913	C_{27}	4.332
n-C_4	0.051	C_{15}	3.870	C_{28}	3.007
i-C_5	0.067	C_{16}	3.016	C_{29}	3.484
n-C_5	0.096	C_{17}	4.321	C_{30}	1.933
i-C_6	0.081	C_{18}	6.668	C_{31}	2.412
n-C_6	0.169	C_{19}	6.064	C_{32}	2.377
C_7	0.729	C_{20}	3.996	C_{33}	3.524
C_8	2.468	C_{21}	4.659	C_{34}	1.257
C_9	1.799	C_{22}	4.967	C_{35}	1.246
C_{10}	2.421	C_{23}	5.806	C_{36}	0.574

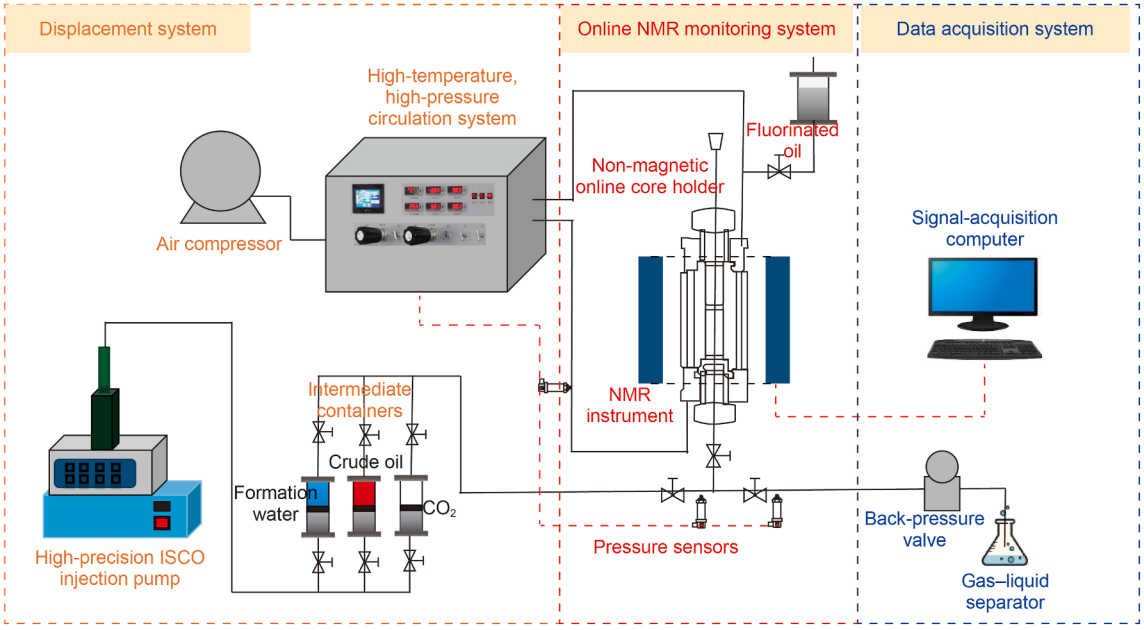

Fig. 4. Schematic diagram of the experimental apparatus for CO_2 huff-n-puff experiments monitored by online NMR technology.

(1) Core pretreatment and baseline NMR scan: Each core was oven-dried to its pre-saturation mass to eliminate signals from bound water protons. An initial T_2 relaxation scan was performed; the resulting signal intensity served as the baseline.
(2) Oil saturation of the core: The core was placed in an intermediate container and was evacuated to −1 MPa for 24 h using a molecular vacuum pump. Dehydrated crude oil was allowed to self-imbibe into the container, which was then pressurized to 40 MPa and was maintained at 363.15 K for at least one week. Following saturation, the T_2 spectrum of the oil saturated core was acquired.
(3) CO_2 huff-n-puff: The saturated core was encapsulated in heat-shrink tubing and was installed in a non-magnetic, high temperature/high pressure core holder. During the "huff" (injection) stage, CO_2 was injected until the system reached the preset injection pressure, and the injection valve was closed. During the "soaking" stage, the core was maintained under closed conditions for 12 h. During the "puff" (production) stage, the injection port was opened, and the back-pressure valve was regulated, allowing pressure to decline to atmospheric pressure. This cycle was repeated four times, and a T_2 spectrum was recorded at the end of each cycle.

All testing was performed under isothermal conditions at 363.15 K, with specific methodologies outlined in Table 4. Meanwhile, slim tube experiments showed that the minimum miscible pressure (MMP) between the crude oil and CO_2 is 22.14 MPa. Therefore, the injection pressure adopted in the CO_2 huff-n-puff experiments is higher than the MMP, indicating that CO_2 and crude oil can reach the miscible state during the displacement process. To ensure consistency of the experimental variables, we used constant pressure injection with an injection volume of 0.4 PV.

2.4. Calculation method of T_2 value and pore size conversion coefficient

The distribution of NMR T_2 spectrum is a critical parameter for characterizing both the pore-structure and fluid-distribution features of reservoir rocks. In core analysis, acquiring the T_2 distribution is relatively rapid, non-destructive, and intuitive; however, T_2 itself does not directly measure pore size. Calibration and

Table 4
CO_2 huff-n-puff experiment plan.

Number	Core No.	Injectionpressure, MPa	Soakingtime, h	Cycle	Back-pressure, MPa	Confining pressure, MPa	Temperature, K
1	#1	24	12	4	27	27	363.15
2	#2	24	12	4	27	27	363.15
3	#3	24	12	4	27	27	363.15
4	#3	24	18	4	27	27	363.15
5	#3	27	12	4	30	30	363.15

conversion using complementary characterization techniques are therefore required. High-pressure mercury intrusion and N_2 adsorption experiments can be cross referenced with NMR data to establish a correspondence between T_2 values and pore size distributions, thereby enabling conversion from a T_2 spectrum to an actual pore size profile.

Therefore, low-temperature nitrogen adsorption is used to calibrate micropores and mesopores, while high-pressure mercury intrusion is employed for macropores. The conversion coefficient (C) is calculated by comparing the pore throat radii at the peak of the mercury-intrusion and nitrogen-adsorption distributions with the relaxation time at the peak amplitude of the T_2 spectrum. According to NMR relaxation theory, the transverse relaxation time T_2 comprises three components, surface relaxation (T_{2S}), bulk relaxation (T_{2B}), and diffusion relaxation (T_{2D}), as expressed in Eq. (1):

$$\frac{1}{T_2}=\frac{1}{T_{2S}}+\frac{1}{T_{2B}}+\frac{1}{T_{2D}}=\rho_2\frac{S}{V}+\frac{1}{T_{2B}}+\frac{D(G\gamma T_E)^2}{12} \tag{1}$$

where T_E represents the echo spacing, ms; ρ_2 represents the surface relaxation rate of the pores, μm/ms; S represents the pore surface area, μm^2; V represents the pore volume, μm^3; D represents the diffusion coefficient of fluid, μm^2/ms; G represents the magnetic field gradient, G/cm; γ represents gyromagnetic ratio of the ^1H nucleus, rad/(s·T).

Under water-saturated conditions, T_{2B} typically ranges from 2 to 3 s, which is much larger than T_2 values. Moreover, in a homogeneous magnetic field (i.e., $G \approx 0$) and with sufficiently short T_E, both bulk relaxation (T_{2B}) and diffusion relaxation (T_{2D}) become negligible. Hence, in Eq. (1) the second and third terms can be ignored

$$\frac{1}{T_2}=\frac{1}{T_{2S}}=\rho_2\frac{S}{V}=\rho_2\frac{F_r}{r} \tag{2}$$

where F_r is the dimensionless geometric shape factor of the pore-throat. For spherical pores, $F_r = 3$; for cylindrical capillaries, $F_r = 2$.

Eq. (2) shows that the transverse relaxation time T_2 of fluid in a pore throat is related both to the pore size and its geometry: the smaller the pore, the shorter the corresponding T_2. Moreover, Eq. (2) establishes a one-to-one correspondence between T_2 and the pore throat radius r. Therefore, it is entirely reasonable to use the NMR T_2 spectrum to quantitatively characterize pore structure. By introducing a conversion coefficient C between T_2 and r, Eq. (2) can be rewritten as follows:

$$r = CT_2 \tag{3}$$

In this study, the NMR T_2 spectral distribution is integrated with high-pressure mercury intrusion and nitrogen adsorption data. Within a common coordinate framework, we fit the pore radii at the peak of the mercury-intrusion saturation-gradient curve and the peak of the nitrogen-adsorption curve against the relaxation time corresponding to the maximum amplitude of the T_2 spectrum. Specifically, for a given water saturation, we extract the matching T_2 spectrum and the pore-throat distribution curves from mercury intrusion and nitrogen adsorption, then perform a linear regression between relaxation time and pore radius to determine the conversion coefficient C for each rock sample.

3. Results and discussion

3.1. Pore size distribution and structural characteristics of different types of oil reservoirs

3.1.1. Analysis of high pressure mercury intrusion results

Fig. 5 presents the capillary pressure curves for the three core samples. Overall, each intrusion curve exhibits a relatively extended plateau region, indicating a concentrated pore size distribution and correspondingly weak heterogeneity in pore diameters. Moreover, all three intrusion curves display a slightly concave shape with modest skewness. Fig. 6 shows the corresponding pore size distribution curves derived from mercury intrusion. All three cores contain predominantly sub-micrometer pores; notably, core #3 exhibits a higher proportion of small pores compared to the other two samples.

The characteristic parameters of the capillary pressure curves are listed in Table 5. The threshold pressures range from 1.500 to 2.397 MPa, corresponding to maximum pore throat radii of 0.31–0.50 μm. The median pressures lie between 6.229 and 9.825 MPa. Overall, the samples from the study area exhibit very small pore throat radii (median radius ≈ 0.075 μm), low mercury extrusion efficiencies (28.77%–38.36%), and good pore throat sorting. Core #1 shows low threshold and median pressures, a relatively large median radius, and facile mercury intrusion and extrusion, yielding the highest extrusion efficiency. This indicates larger pore throat sizes, simpler pore architecture, and good overall connectivity, with minimal bottleneck effects during mercury ingress and egress. However, its higher sorting coefficient also suggests a relatively broad pore size distribution, with a proportion of finer throats present alongside larger pores. Cores #2 and #3 have higher threshold and median pressures and smaller median radii, requiring greater pressure for mercury intrusion and displaying lower extrusion efficiencies. This reflects smaller, more complex throats with more narrow bottleneck pores that trap mercury more readily.

3.1.2. Analysis of nitrogen adsorption results

Fig. 7 is the nitrogen adsorption and desorption isotherms for the three core samples. Overall, the desorption curves run nearly parallel to the adsorption curves, producing narrow, elongated hysteresis loops with relatively small loop areas—characteristic of type H3 hysteresis. This suggests that the pore structures in these shales resemble parallel plate or slit shaped pores, which are typically open and favorable for fluid flow. Although all three cores exhibit H3 type hysteresis, their adsorption capacities and loop areas differ: Core #1 displays significantly higher adsorption

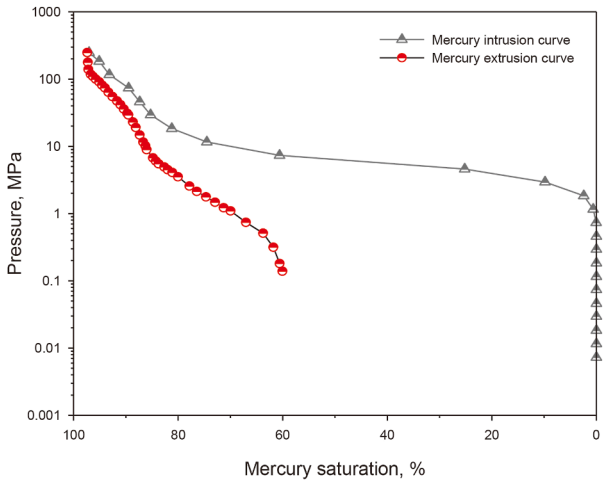

(a) Core #1

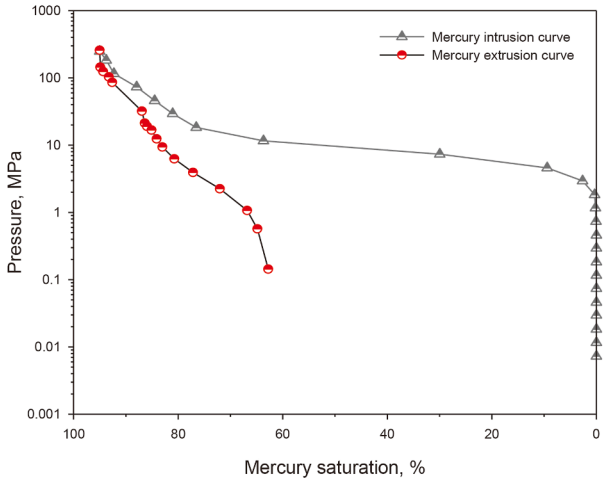

(b) Core #2

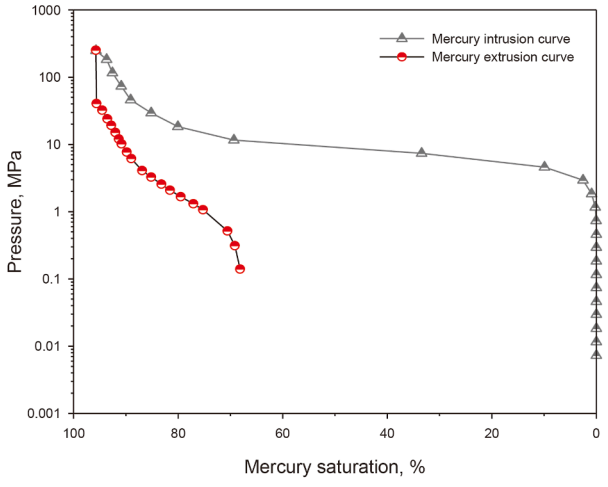

(c) Core #3

Fig. 5. High pressure mercury injection capillary pressure curves of different types of oil reservoirs.

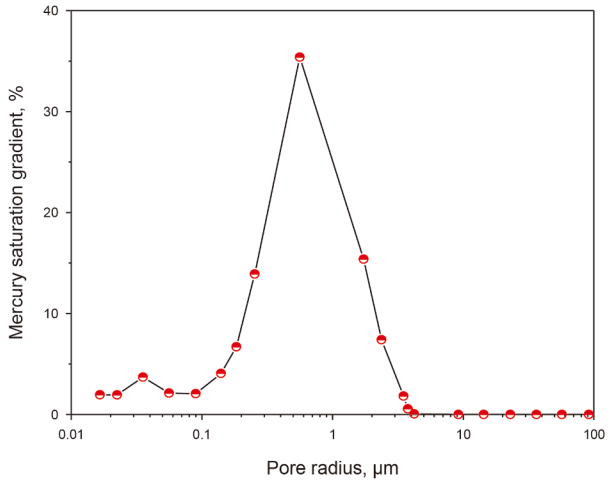

(a) Core #1

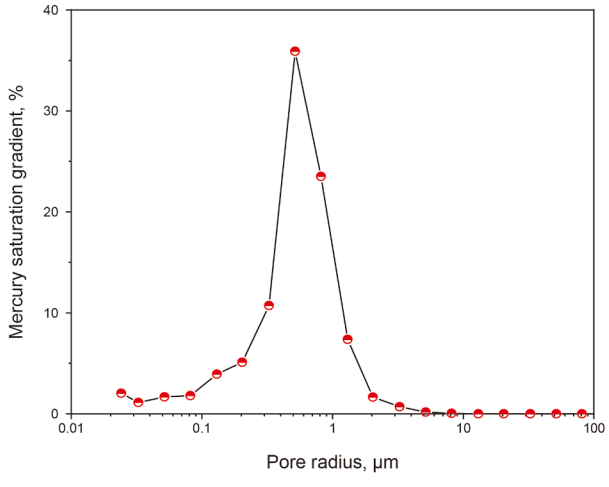

(b) Core #2

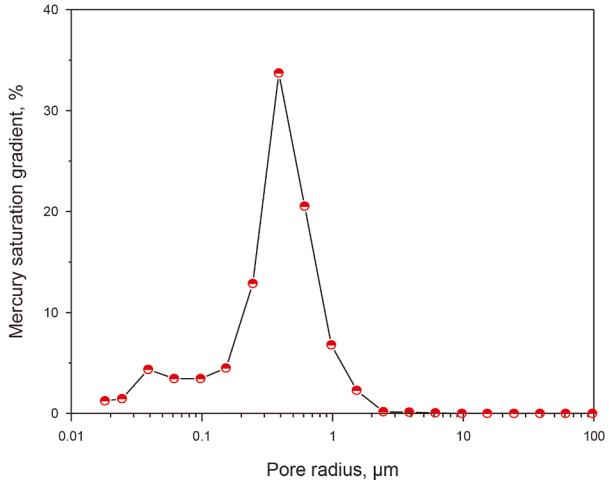

(c) Core #3

Fig. 6. High pressure mercury injection pore size distribution curves of different types of oil reservoirs.

Table 5
Characteristic parameters of capillary pressure curves.

Core No.	Threshold pressure, MPa	Median pressure, MPa	Maximum intrusion saturation, %	Mean coefficient	Average pore radius, μm	Median pore radius, μm	Extrusion efficiency, %	Sorting coefficient
#1	1.505	6.229	97.054	12.768	0.038	0.114	38.356	1.526
#2	2.002	9.212	95.771	13.102	0.039	0.080	33.760	1.286
#3	2.397	9.825	95.011	13.232	0.035	0.075	28.768	1.317

volume and a larger hysteresis loop area than Cores #2 and #3, indicating a relatively greater total porosity.

Fig. 8 shows the pore-size distributions of the three core samples calculated using density functional theory (DFT). The core assumption of DFT is that all properties of a system (e.g., energy, charge density, etc.) are uniquely determined by its electron density. In analyses of fluid adsorption in porous materials, this framework is extended to consider the spatial distribution of fluid density. By solving the adsorption integral equation (Eq. (4)), the fluid distribution within pores under various conditions can be obtained, thereby deriving the pore size distribution.

$$N(P/P_0) = \int_{H_{\min}}^{H_{\max}} v(P/P_0, H) f(H) \mathrm{d}H \tag{4}$$

where $N(P/P_0)$ is the excess adsorption at relative pressure P/P_0, cm^3/g; $v(P/P_0, H)$ is the kernel function describing the relationship between excess adsorption and pore size (H) and relative pressure (P/P_0), cm^3/cm^3; and $f(H)$ is the pore size distribution, $cm^3/(g{\cdot}nm)$.

The pore sizes of all three cores are predominantly concentrated in the mesopore range, particularly below 15 nm, and their distribution curves exhibit a unimodal shape, indicating relatively uniform pore sizes.

3.1.3. Determination of the pore radius conversion coefficient

Fig. 9 is the determination curves of the conversion coefficient (C) for the three core samples, integrating N_2 adsorption, high-pressure mercury intrusion, and NMR T_2 spectra. As shown in Fig. 9, pore size distributions derived from nitrogen adsorption and Hg intrusion exhibit strong alignment with NMR relaxation time trends. The nitrogen adsorption data are predominantly within the 0.1–1 ms relaxation time range, characterizing the small pores, whereas the mercury intrusion data range from 1 to 100 ms, reflecting the large pores. By fitting T_2 relaxation times to corresponding pore radii, the conversion coefficients (C) were found to be 0.0389 μm/ms for core #1, 0.0398 μm/ms for core #2, and 0.0390 μm/ms for core #3.

To simplify the analysis, in this study pore radii are classified into three categories (Wang et al., 2021): small pores (< 50 nm), medium pores (50–300 nm), and large pores (> 300 nm). The converted pore size distribution curves and proportion of pore size are shown in Fig. 10. Statistical results indicate that the shale cores from the Jimusar reservoir in Xinjiang are dominated by medium pores, with overall small pore radii. For the Type I oil reservoir class (core #1), small pores account for 5.52%, medium pores 71.85%, and large pores 22.63%; for the Type II oil reservoir class (core #2), small pores account for 8.52%, medium pores 72.85%, and large pores 18.63%; and for the Type III oil reservoir class (core #3), small pores account for 44.61%, medium pores 49.56%, and large pores 5.83%.

3.2. Oil recovery of CO_2 huff-n-puff

The NMR T_2 spectrum can characterize the distribution of fluids within pores of different sizes in the shale cores. The amplitude of the T_2 spectrum signal is directly proportional to the volume of fluid occupying the pores: a larger signal indicates a greater fluid content. Therefore, by tracking changes in the T_2 spectrum over successive cycles, one can quantify the recovery degree for each cycle. The calculation is given by the following formula:

$$R = \left(1 - \frac{S_{\text{after}}}{S_{\text{before}}}\right) \times 100\% \tag{5}$$

where R is the oil recovery; S_{after} is the T_2 spectrum signal after CO_2 huff-n-puff; S_{before} is the T_2 spectrum signal in the oil-saturated state.

Based on the NMR T_2 distributions for the individual stages of CO_2 huff-n-puff shown in Fig. 11 and applying Eq. (5), the oil recovery after four cycles reaches 56.09% for the Type I reservoir, 46.81% for the Type II reservoir, and 28.30% for the Type III reservoir. As shown in Fig. 12, for the Type I reservoir, the first, second, third, and fourth cycles contribute 26.04%, 19.70%, 6.57%, and 3.78% of the total recovery, respectively. For the Type II reservoir, the contributions of cycles 1–4 are 25.68%, 13.57%, 4.76%, and 2.80%, respectively. For the Type III reservoir, cycles 1–4 contribute 9.25%, 8.19%, 5.47%, and 5.39%, respectively.

These results indicate that in the Type I and Type II reservoirs, productivity gains are pronounced during the first two cycles, whereas subsequent cycles yield diminishing returns reflecting better reservoir properties and high oil mobility. In contrast, the Type III reservoir still produces substantial additional oil in the third and fourth cycles, implying that multiple huff-n-puff cycles can effectively enhance recovery in poorer reservoir petrophysical properties.

Figs. 2 and 3 show, respectively, the mineral compositions and pore type assemblages of the three types of oil reservoirs. All three types of oil reservoirs share the common features of high feldspar (dominated by plagioclase) and dolomite contents and very low clay content, but they differ systematically in the quartz carbonate proportions and in pore structure: The Type I reservoir is a dolomitic sandstone in which residual intergranular pores and intergranular dissolution pores predominate; pore sizes are relatively large and the pore connectivity is good. The Type II reservoir is a dolomitic fine siltstone, characterized by the coexistence of intergranular dissolution pores and intragranular dissolution

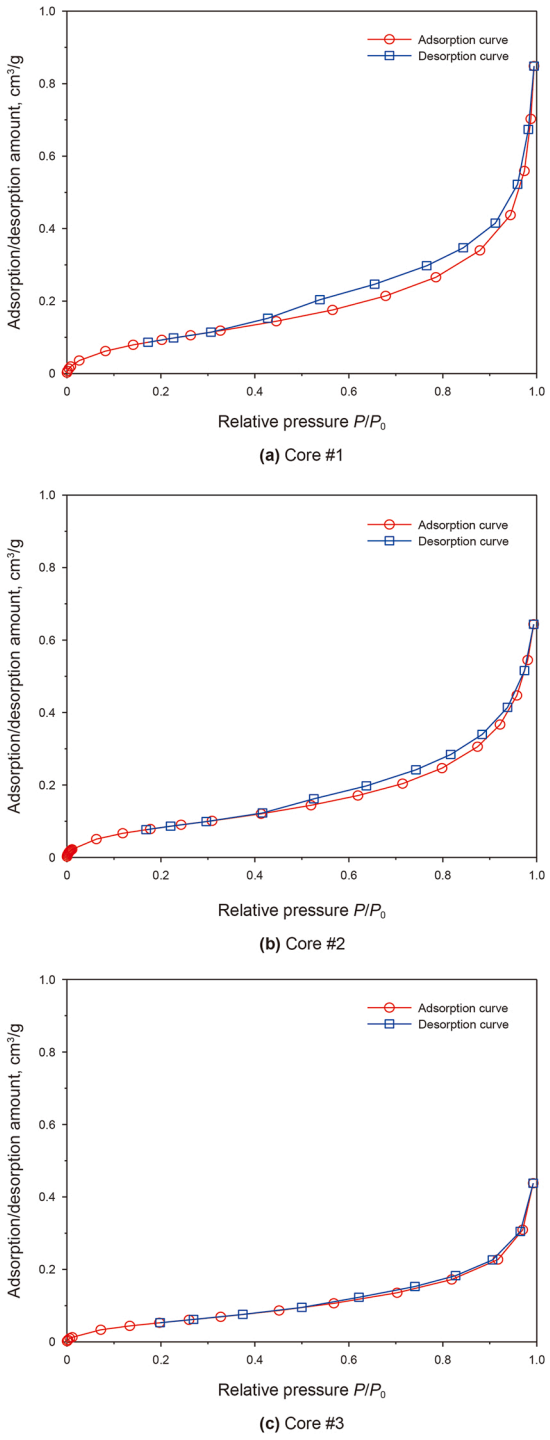

Fig. 7. Adsorption and desorption curves of different types of oil reservoirs.

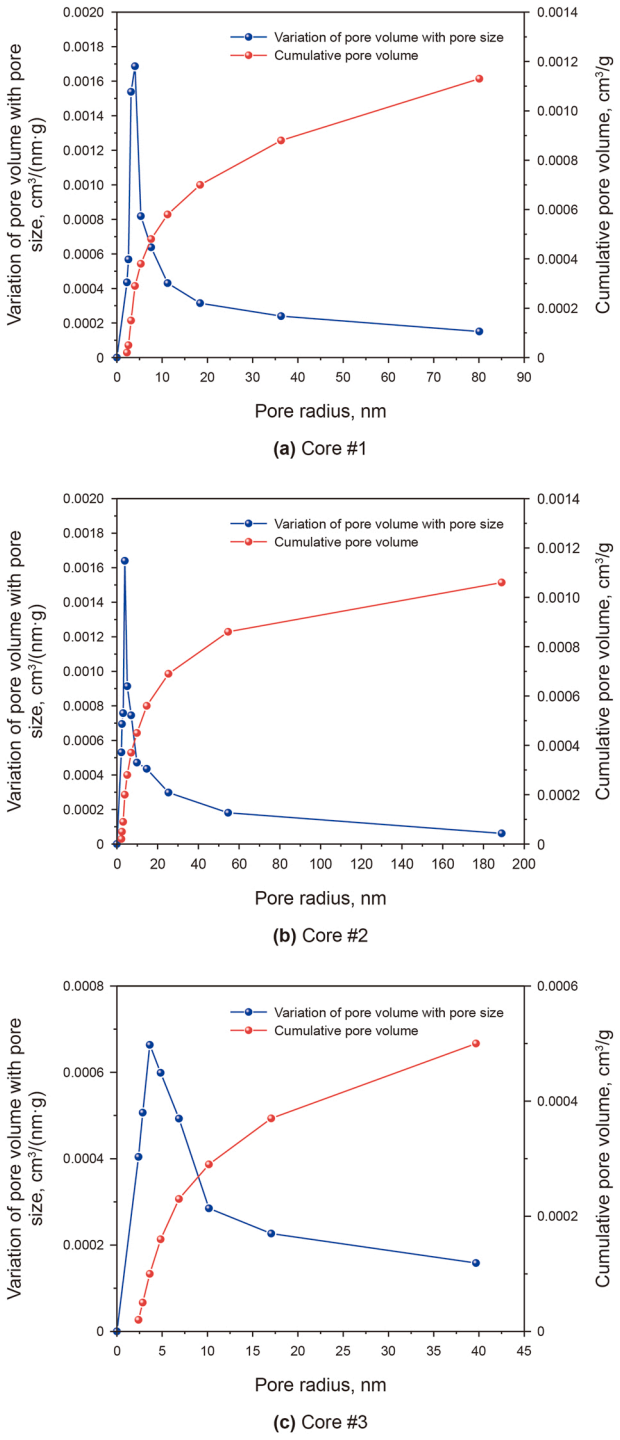

Fig. 8. The pore size distribution curves of different types of oil reservoirs.

pores, i.e., a "large pore but narrow throat" fabric. The Type III reservoir is an argillaceous fine siltstone, dominated by intragranular dissolution pores with only minor intergranular dissolution pores; pore throats are slender, and connectivity is poor. Consequently, the CO_2 huff-and-puff recovery is highest in the Type I reservoir and second highest in the Type II reservoir, indicating that pore size, connectivity, and mineral composition are the primary controls on huff-n-puff performance. Mechanistically, micron scale intergranular pores and well connected intergranular dissolution pores have low capillary pressures and high connectivity, allowing CO_2 to readily invade and dissolve/swell the oil, reduce viscosity, and extract light components, leading to convection dominated rapid mobilization; in contrast, nano- to micron-scale intragranular dissolution pores are commonly isolated or linked by fine throats, with high capillary resistance and oil mainly in adsorbed/immobile states, so mobilization relies on

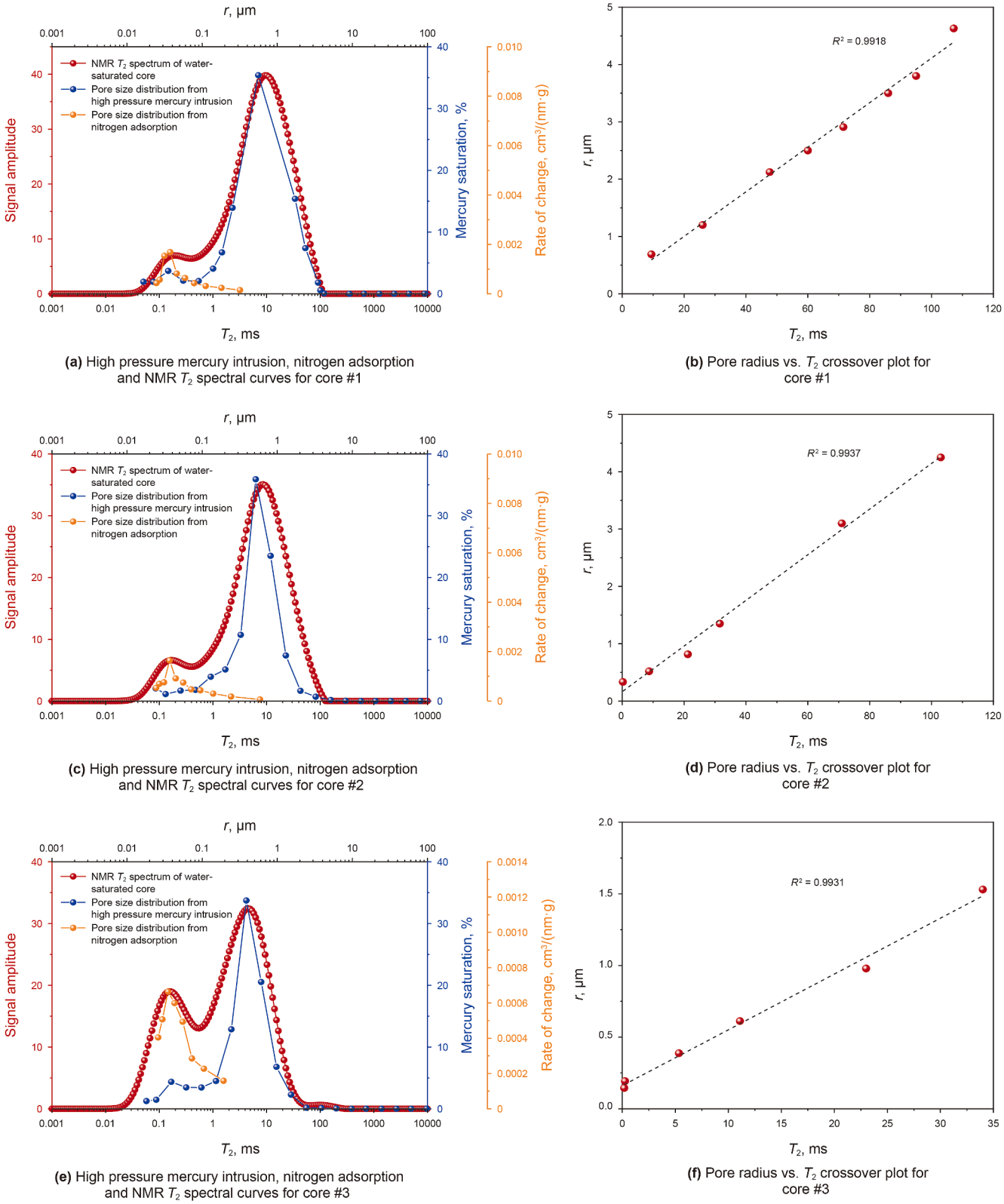

(a) High pressure mercury intrusion, nitrogen adsorption and NMR T_2 spectral curves for core #1

(b) Pore radius vs. T_2 crossover plot for core #1

(c) High pressure mercury intrusion, nitrogen adsorption and NMR T_2 spectral curves for core #2

(d) Pore radius vs. T_2 crossover plot for core #2

(e) High pressure mercury intrusion, nitrogen adsorption and NMR T_2 spectral curves for core #3

(f) Pore radius vs. T_2 crossover plot for core #3

Fig. 9. High pressure mercury intrusion–nitrogen adsorption–NMR T_2 spectrum fitting curves.

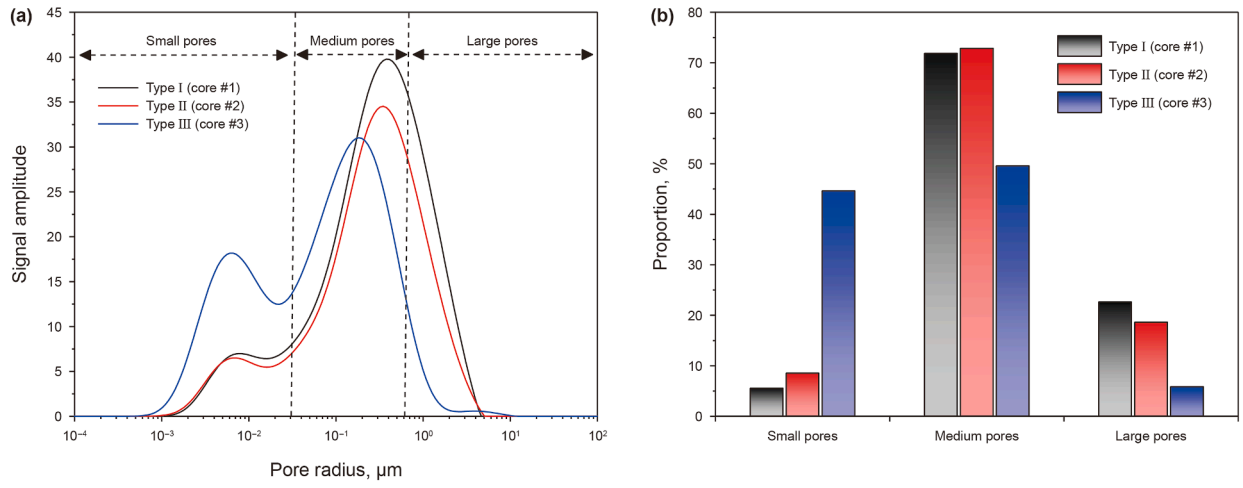

(a) Pore distribution **(b)** Proportion of pore size

Fig. 10. Converted pore size distribution curves and proportion of pore size.

diffusion and competitive adsorption. In terms of mineralogy, dolomite and quartz enhance rock brittleness and help preserve dissolution pores, microfractures, and intergranular pores, thereby expanding the effective CO_2 sweep. In summary, the general mineral composition–pore type–CO_2 huff-n-puff relationship is as follows: when feldspar (especially plagioclase) is abundant, the rock is also enriched in brittle minerals (quartz and dolomite), and the pore system is dominated by intergranular dissolution pores, the reservoir exhibits good connectivity, convection dominated flow, and a strong huff-n-puff response; by contrast, when feldspar (especially plagioclase) is dominant but the pore system is dominated by intragranular (intraparticle) dissolution pores, connectivity is poor, transport is diffusion dominated, and the response is weak.

According to Table 4, CO_2 huff-n-puff tests were conducted on the Type III oil reservoir class (core #3) under different parameters, including injection pressures and soaking times, to elucidate the effects of these parameters on the oil recovery.

When the injection pressure increased from 24 to 27 MPa, as shown in Fig. 13, the cumulative oil recovery in the Type III oil reservoir class rose from 28.30% to 32.37%. Analysis of recovery contributions by pore class (large, medium, and small) indicates that the gain in recovery is primarily attributable to enhanced mobilization of medium- and large-sized pores.

As the soaking time was elevated from 12 to 18 h, as shown in Fig. 14, the cumulative oil recovery in the Type III oil reservoir class rose modestly from 28.30% to 29.36%. Analysis of oil recovery of different pores indicates that the incremental gain predominantly occurs in the small pores, demonstrating that extended soaking time chiefly enhances oil mobilization within the smallest pores.

In summary, field applications should first increase injection pressure to mobilize oil in medium to large pores and capture the main gains. Subsequently, soaking time can be judiciously extended to fully mobilize oil in smaller pores—an approach better suited to mid-to-late stages or lower quality reservoir.

3.3. Lower limits of oil mobilization pore radii for CO_2 huff-n-puff

By comparing the NMR T_2 spectra of the core in its initial oil saturated state with those obtained after four cycles, one can identify the smallest pore sizes that CO_2 can mobilize, as well as the primary pores contributing to recovery. From the recovery curve derived from Fig. 11, we compute the first and second order derivatives and compare them against the pore size distribution measured under oil saturated conditions to control for the influence of the pore volume distribution. As a preliminary analysis, this study focuses on the morphological features of the derivative curves.

In addition to the first order derivative of the oil recovery curve, we further analyze its second order derivative to determine the lower limit of pore radii for oil mobilization. This approach reduces subjective “by eye” picking on a broad first order derivative shoulder and provides a reproducible, quantitative criterion for the cutoff pore radius, which is particularly important in tight/shale reservoirs where noisy data and multiple local maxima can obscure the true onset of oil mobilization.

(1) When the second order derivative first changes from zero to positive as the recovery curve starts to deviate from zero, it marks the onset of effective pore mobilization. The corresponding pore radius is taken as the lower limit pore radius for oil mobilization.
(2) When the second order derivative transitions from positive to negative (i.e., at an inflection point of the recovery curve with respect to the linear pore radius), the first order derivative reaches a local maximum. This maximum of the first order derivative identifies the pore size that contributes the most to the incremental oil recovery: As the pore radius continues to increase beyond this value, the oil recovery still increases (the first order derivative remains positive), but the incremental contribution per unit increase in pore

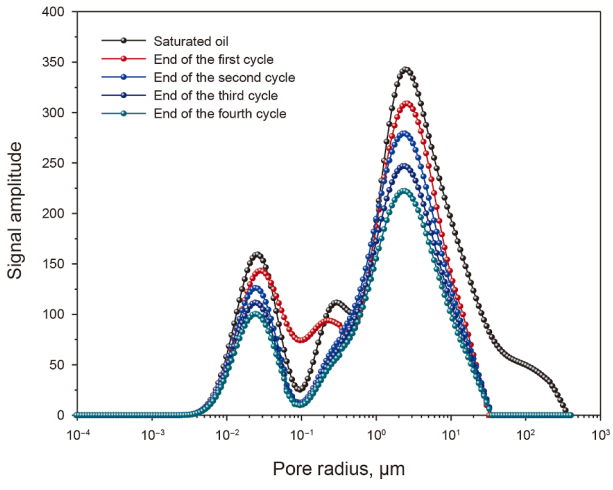

(a) Type I (core #1)

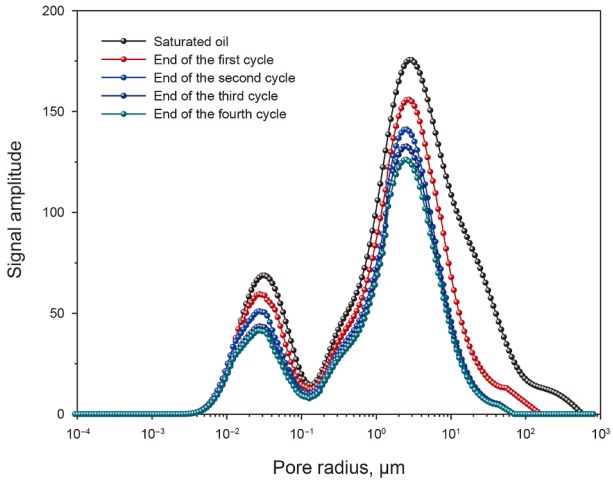

(b) Type II (core #2)

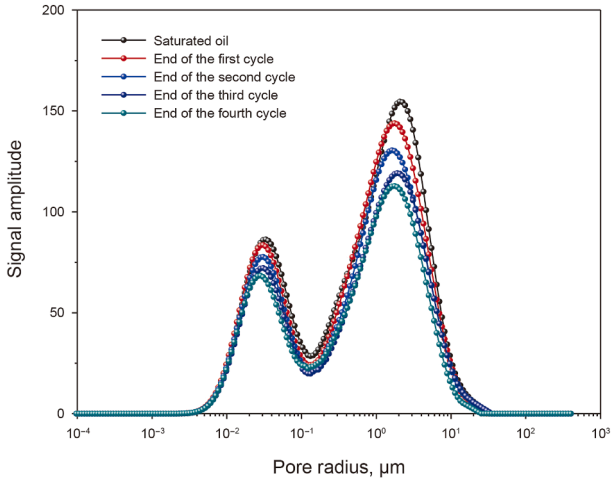

(c) Type III (core #3)

Fig. 11. T_2 spectra at different stages of CO_2 huff-n-puff.

radius gradually decreases. The corresponding pore radius therefore represents the dominant contribution pore size, rather than implying that only pores larger than this radius participates in flow.

As shown in Fig. 15, the lower limits of oil mobilization pore radii for CO_2 huff-n-puff in the Jimusar shale oil reservoir range from 20 to 35 nm. For the samples in this study, the peak of the first order derivative does not coincide exactly with the peak of the pore size distribution curve, indicating that the pore size making the largest incremental contribution to oil recovery is jointly controlled by pore abundance and pore connectivity, with pore connectivity exerting a particularly important influence, rather than by pore abundance alone. In the Type I oil reservoir class, after four cycles of CO_2 huff-n-puff, oil in pores larger than 20 nm becomes mobilizable, and the pore size making the largest incremental contribution to oil recovery is approximately 160 nm. In the Type II oil reservoir class, the initial mobilization threshold rises to pores larger than 28 nm before noticeable oil movement occurs, with the strongest contribution to oil recovery coming from pores around 180 nm. In the Type III oil reservoir class, pore mobilization does not begin until pore radii reach 35 nm, and the pore size that contributes most to the incremental oil recovery is approximately 200 nm.

Based on the mercury intrusion curves (as shown in Fig. 5) and pore type characteristics of the three oil reservoir classes, the differences in the “lower limit of mobilization pore radius” can be attributed to the coupled effects of capillary pressure, connectivity, and nanoscale rheology. Type I oil reservoir class exhibits mercury intrusion curves with lower threshold and median pressures and relatively larger median radii; along the critical displacement path, the minimum throat radius is larger, and the number of narrow bottlenecks is smaller, so flow pathways can form under lower capillary resistance, yielding the lowest mobilization cutoff. Type II oil reservoir class shows higher threshold and median pressures, with a greater proportion of medium-small pore throats. Connectivity is governed by the minimum throat bottleneck, the number of flow channels decreases, and the critical paths become slenderer; consequently, at the same driving pressure differential it is still insufficient to overcome the higher capillary pressure and viscous dissipation, so the mobilization cutoff is higher than in Type I. Type III oil reservoir class is dominated by medium-small throats and has weaker connectivity; flow channels are narrow and discontinuous, leading to strong capillary sealing and pronounced “intermittent connectivity.” In terms of capillarity and connectivity, the Young–Laplace law indicates that the capillary pressure rises as the pore radius decreases; fluid flow must then overcome greater resistance while reduced connectivity further limits the number of flow paths. From the nanoscale rheology perspective, the oil viscosity in confinement exceeds the bulk value, the slip length decreases, and the interfacial dissipation is enhanced by roughness and chemical heterogeneity, making it harder for the capillary number, at the same flow rate, to surpass the mobilization threshold.

In a word, across the three oil reservoir classes, the lower limit of mobilization pore radius increases with greater pore throat complexity and decreases with poorer connectivity, reflecting the combined amplification of capillary pressure increases, weakened connectivity, and adverse nanoscale rheology.

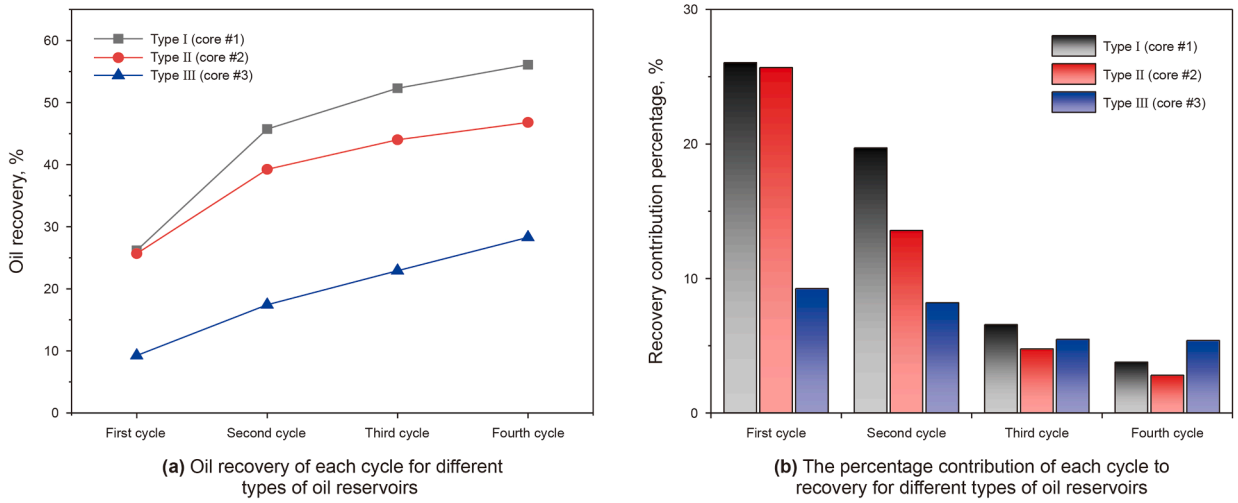

(a) Oil recovery of each cycle for different types of oil reservoirs

(b) The percentage contribution of each cycle to recovery for different types of oil reservoirs

Fig. 12. Oil recovery in each cycle and the percentage contribution of each cycle.

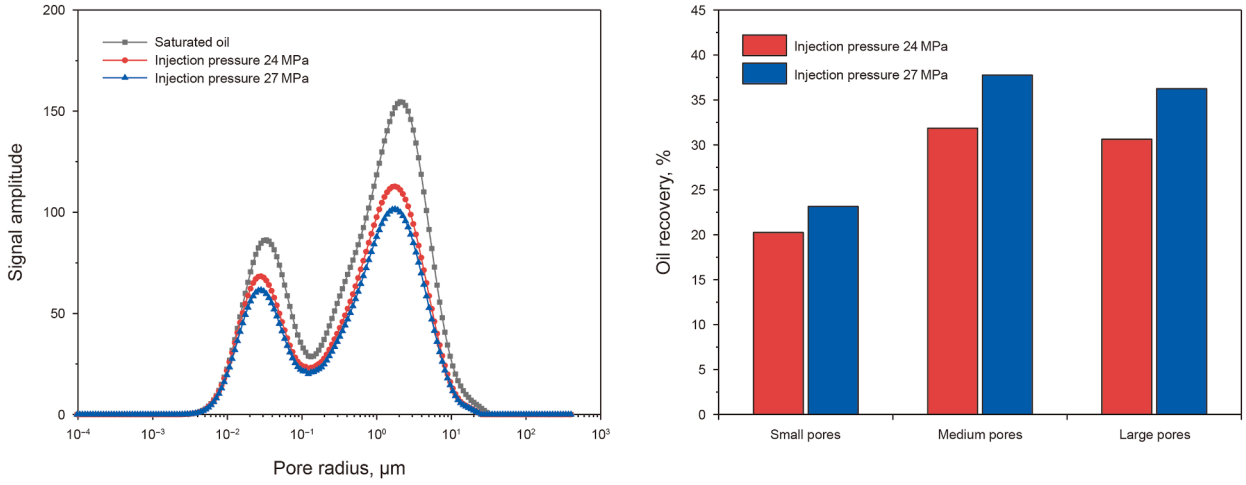

(a) T_2 spectral distribution

(b) Oil recovery

Fig. 13. Distribution of T_2 spectra and oil recovery under different injection pressures.

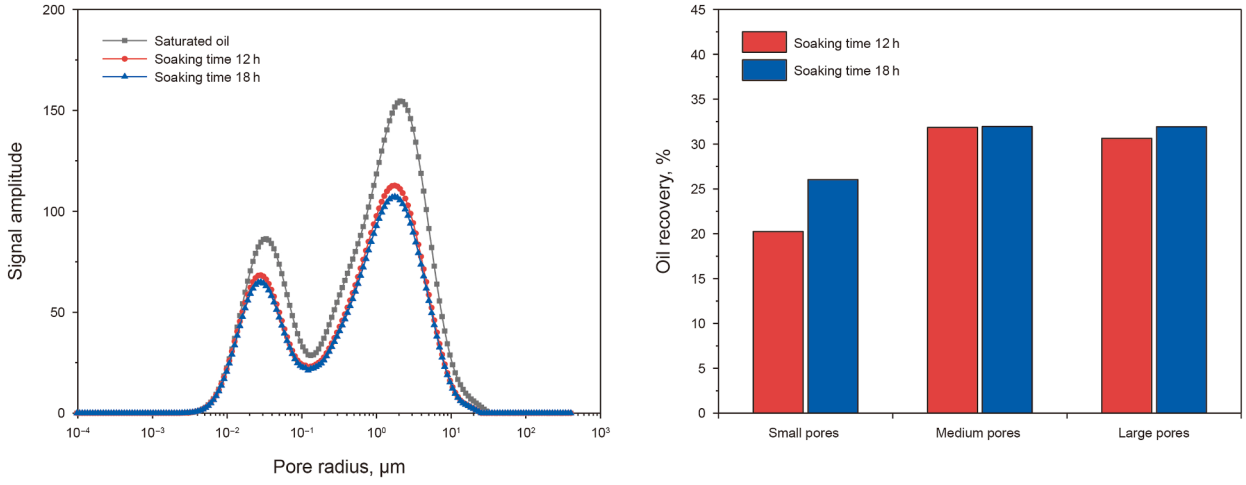

(a) T_2 spectral distribution

(b) Oil recovery

Fig. 14. Distribution of T_2 spectra and oil recovery under different soaking times.

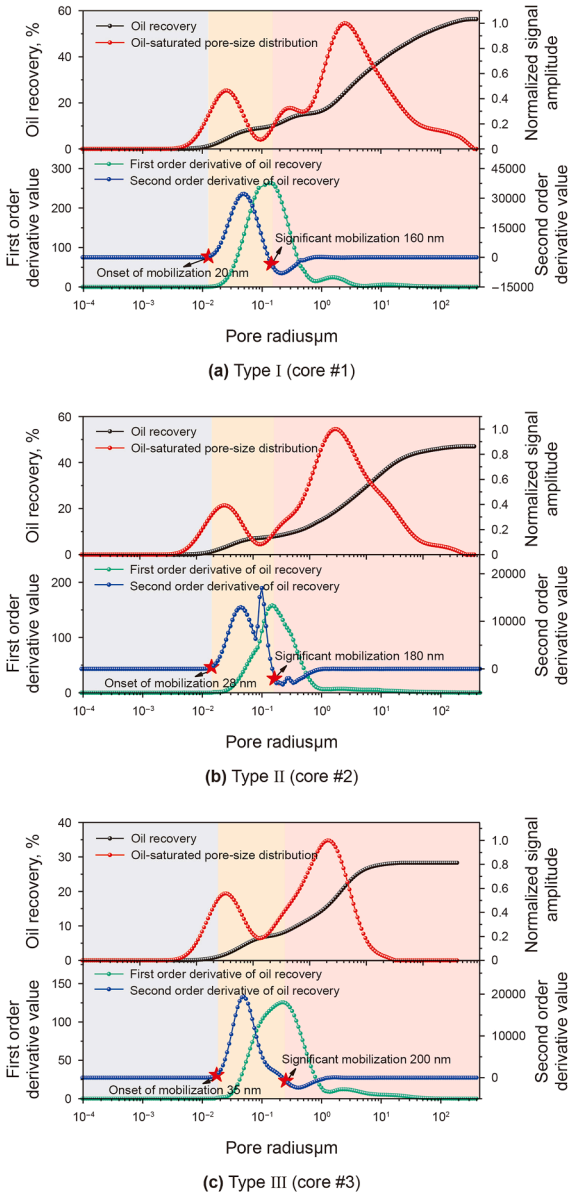

Fig. 15. Oil recovery, oil saturated pore size distribution, the first and second order derivative curves after four cycles of CO_2 huff-n-puff. (i) The first order derivative is computed with respect to the linear pore radius using finite differences. (ii) The logarithmic *x* axis in Fig. 15 is used only for visualization and does not imply that the derivative represents the slope with respect to lgr.

Same as in Section 3.2, the influence of different injection pressures and soaking times on the lower limits of oil mobilization pore radii was investigated. As shown in Fig. 16, when the injection pressure increases from 24 to 27 MPa, the lower limit of oil mobilization pore radii in the Type III oil reservoir class decreases from 35 to 30 nm; when the soaking time increases from 12 to 18 h, the lower limit in the Type III oil reservoir class decreases from 35 to 33 nm.

4. Conclusions

Based on high-pressure mercury intrusion, nitrogen adsorption, and NMR experiments, this study established a methodology for characterizing the pore structures of the Jimusar shale and determined the lower limits of oil mobilization pore radii and oil recovery for CO_2 huff-n-puff. The main conclusions are as follows:

(1) The mercury intrusion curves for cores #1, #2, and #3 all exhibit a slightly concave shape with modest skewness. Their nitrogen adsorption isotherms display type H3 hysteresis loops that are narrow and elongated with small loop areas, indicating uniform pore structures, good connectivity, and predominantly open pores favorable for shale oil flow.

(2) All oil reservoir classes are dominated by medium pores. In the Type I oil reservoir class (core #1), small pores account for 8.52%, medium pores for 72.85%, and large pores for 18.63%. In the Type II oil reservoir class (core #2), small pores account for 6.52%, medium pores for 70.85%, and large pores for 22.63%. In the Type III oil reservoir class (core #3), small pores account for 44.61%, medium pores for 49.56%, and large pores for 5.83%.

(3) After four cycles, the cumulative oil recovery is 56.36% for the Type I oil reservoir class, 46.81% for Type II, and 28.30% for Type III. Using an innovative second order derivative method based on oil recovery, the lower limits of oil mobilization pore radii to production for CO_2 huff-n-puff in the Jimusar shale range from 20 to 35 nm.

(4) The oil recovery is enhanced by 4.07% when the injection pressure is increased from 24 to 27 MPa. This is achieved primarily by mobilizing oil from large and medium pores and reducing the lower mobilization limit of pore radius by 5 nm. Extending the soaking time from 12 to 18 h marginally enhances oil recovery by 1.06%. This extension primarily mobilizes oil contained within smaller pores and decreases the lower limit of oil mobilization pore radius to production by approximately 2 nm.

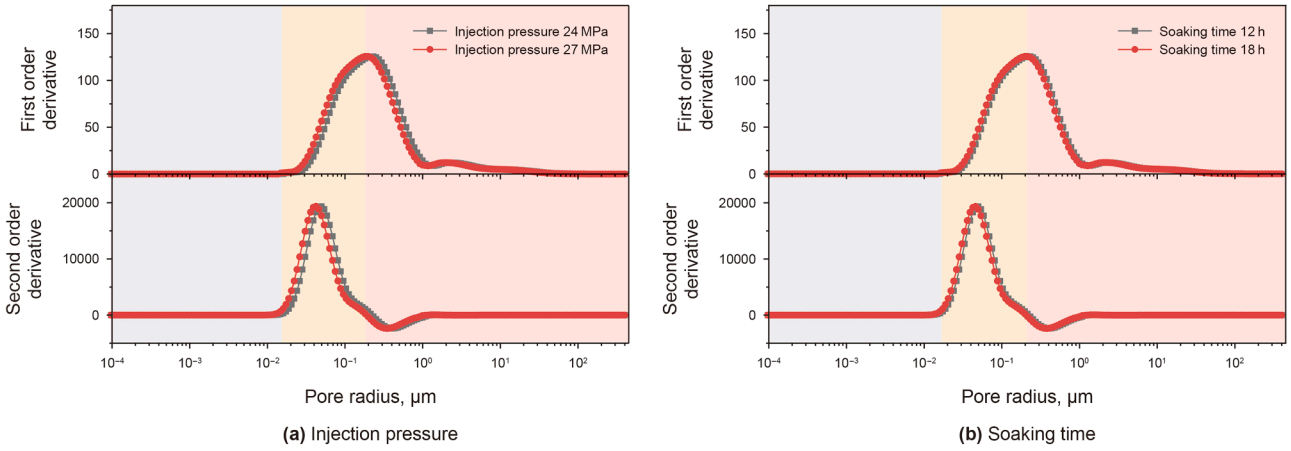

Fig. 16. The first and second order derivative curves under different parameters.

CRediT authorship contribution statement

Qing Li: Writing – original draft, Visualization, Formal analysis. **Ying-Yan Li:** Visualization, Validation, Methodology. **Pei-Yu Li:** Writing – review & editing, Validation, Conceptualization. **Ji-Xiang He:** Resources, Investigation, Data curation. **Yi-Lei Song:** Writing – review & editing, Supervision. **Chi-Yang Yu:** Software, Methodology. **Zhao-Jie Song:** Supervision, Funding acquisition, Conceptualization. **Hao-Chen Ren:** Writing – review & editing.

Declaration of competing interest

The authors declare that they have no known competing financial interests or personal relationships that could have appeared to influence the work reported in this paper.

Acknowledgements

This research was supported by the National Science and Technology Major Project (2025ZD1405003), National Natural Science Foundation of China (52074319), Natural Science Foundation of Xinjiang Uygur Autonomous (2025D01B196), Strategic Cooperation Technology Project of CNPC (ZLZX2020-01-08), and Special Project of CNPC (2023ZZ15YJ04).

References

Chen, L., He, A., Zhao, J., Kang, Q., Li, Z., Carmeliet, J., Shikazono, N., Tao, W., 2022. Pore-scale modeling of complex transport phenomena in porous media. Prog. Energ. Combust. 88, 100968. https://doi.org/10.1016/j.pecs.2021.100968.

Chen, Y., Zhi, D., Qin, J., Song, P., Zhao, H., Wang, F., 2022. Experimental study of spontaneous imbibition and CO_2 huff and puff in shale oil reservoirs with NMR. J. Petrol. Sci. Eng. 209, 109883. https://doi.org/10.1016/j.petrol.2021.109883.

Clarkson, C.R., Freeman, M., He, L., Agamalian, M., Melnichenko, Y.B., Mastalerz, M., Bustin, R.M., Radliński, A.P., Blach, T.P., 2012. Characterization of tight gas reservoir pore structure using USANS/SANS and gas adsorption analysis. Fuel 95, 371–385. https://doi.org/10.1016/j.fuel.2011.12.010.

Gao, Y., Liu, D., Li, S., Cheng, L., Sun, J., 2024. Optimization of CO_2 injection huff and puff process in shale reservoirs based on NMR technology. Appl. Sci. 14 (6), 2411. https://doi.org/10.3390/app14062411.

Ge, X., Fan, Y., Deng, S., Han, Y., Liu, J., 2016. An improvement of the fractal theory and its application in pore structure evaluation and permeability estimation. J. Geophys. Res. Solid Earth 121 (9), 6333–6345. https://doi.org/10.1002/2016JB013074.

Gong, H., Zhang, H., Lv, W., Xu, L., Li, Z., Dong, M., 2022. Effects of kerogen on the flow and EOR performance of oil in shale cores during CO_2 flooding process investigated by NMR technology. SPE J. 27 (4), 2244–2256. https://doi.org/10.2118/209581-PA.

Han, X., Song, Z., Deng, S., Li, B., Li, P., Lan, Y., Song, Y., Zhang, L., Zhang, K., Zhang, Y., 2024. Multiphase behavior and fluid flow of oil–CO_2–water in shale oil reservoirs: Implication for CO_2-water-alternating-gas huff-n-puff. Phys. Fluids 36 (6), 063310. https://doi.org/10.1063/5.0213861.

Han, Y., Lei, Z., Wang, C., Liu, Y., Liu, J., Du, P., Wang, Y., Liu, P., 2024. A novel multiphase and multicomponent model for simulating molecular diffusion in shale oil reservoirs with complex fracture networks. Phys. Fluids 36 (5), 056105. https://doi.org/10.1063/5.0205812.

Hartono, K.F., Permadi, A.K., Paryoto, S., Resha, A.H., Pratiwi, R., Prakoso, S., Djumantara, M., 2024. The characteristics of produced oils in the miscible CO_2 displacement process. In: IOP Conf. Ser. Earth Environ. Sci. https://doi.org/10.1088/1755-1315/1339/1/012021.

He, X., Luo, Q., Li, X., Jiang, Z., Liang, C., Qiu, Z., Li, Y., Deng, Y., 2025. Microscopic occurrence mechanism of shale oil in saline lacustrine shale: Insights from NMR and micro-CT combined with saturated oil, centrifuged and solvent extraction experiments. Nat. Resour. Res. 34, 2089–2116. https://doi.org/10.1007/s11053-025-10486-x.

He, Y., Wei, B., Zhao, J., You, J., Kadet, V., Lu, J., 2024. Accurate determination of nano-confined minimum-miscible-pressure to aid CO_2 enhanced oil recovery and storage in unconventional reservoirs. Adv. Geo-Energy. Res. 12 (2), 141–155. https://doi.org/10.46690/ager.2024.05.06.

Kelly, S., El-Sobky, H., Torres-Verdín, C., Balhoff, M.T., 2016. Assessing the utility of FIB-SEM images for shale digital rock physics. Adv. Water Resour. 95, 302–316. https://doi.org/10.1016/j.advwatres.2015.06.010.

Li, L., Su, Y., Sheng, J.J., Hao, Y., Wang, W., Lv, Y., Zhao, Q., Wang, H., 2019a. Experimental and numerical study on CO_2 sweep volume during CO_2 huff-n-puff enhanced oil recovery process in shale oil reservoirs. Energy Fuels 33 (5), 4017–4032. https://doi.org/10.1021/acs.energyfuels.9b00164.

Li, L., Wang, C., Li, D., Fu, J., Su, Y., Lv, Y., 2019b. Experimental investigation of shale oil recovery from Qianjiang core samples by the CO_2 huff-n-puff EOR method. RSC Adv. 9 (49), 28857–28869. https://doi.org/10.1039/C9RA05347F.

Li, L., Zhang, D., Su, Y., Zhang, X., Lu, M., Wang, H., 2024. Microfluidic insights into CO_2 sequestration and enhanced oil recovery in laminated shale reservoirs: Post-fracturing interface dynamics and micro-scale mechanisms. Adv. Geo-Energy. Res. 13 (3), 203–217. https://doi.org/10.46690/ager.2024.09.06.

Li, P., Song, Y., Jiang, J., Song, Z., Han, X., Wang, X., Ren, H., He, J., 2025. Pore-scale simulation of oil-water flow in shale media after fracture hits: An integrated approach using U-net and lattice Boltzmann method. Fuel 402, 136038. https://doi.org/10.1016/j.fuel.2025.136038.

Lv, J., Hu, T., Zhang, W., Jiang, F., Xue, J., Zhang, C., Qi, Z., Huang, R., Hu, M., Jiang, S., 2025. Microscopic oil occurrence in the Permian alkaline lacustrine shales: Fengcheng formation, Mahu Sag, Junggar basin. Pet. Sci. 22 (4), 1407–1427. https://doi.org/10.1016/j.petsci.2025.01.005.

Meng, Y., Song, Z., Song, Y., Zhang, Y., 2024. The impact of porous structure on oil–water two-phase flow under CO_2 environment in continental shale reservoirs. Phys. Fluids 36 (6), 063322. https://doi.org/10.1063/5.0209271.

Pan, Y., Huang, Z., Guo, X., Liu, B., Wang, G., Xu, X., 2022. Study on the pore structure, fluid mobility, and oiliness of the lacustrine organic-rich shale affected by volcanic ash from the Permian Lucaogou Formation in the Santanghu Basin, Northwest China. J. Petrol. Sci. Eng. 208, 109351. https://doi.org/10.1016/j.petrol.2021.109351.

Pang, X., Wang, G., Kuang, L., Lai, J., Gao, Y., Zhao, Y., Li, H., Wang, S., Bao, M., Liu, S., Liu, B., 2022. Prediction of multiscale laminae structure and reservoir quality in fine-grained sedimentary rocks: The Permian Lucaogou Formation in Jimusar Sag, Junggar Basin. Pet. Sci. 19 (6), 2549–2571. https://doi.org/10.1016/j.petsci.2022.08.001.

Shen, Z., Sheng, J.J., 2017. Experimental study of permeability reduction and pore size distribution change due to asphaltene deposition during CO_2 huff and puff injection in Eagle Ford shale. Asia Pac. J. Chem. Eng. 12 (3), 381–390. https://doi.org/10.1002/apj.2080.

Shi, Y., Wu, B., Wang, H., Li, Y., Liu, Z., Xu, C., Qin, J., Li, Y., Song, Z., Liu, H., 2024. Insights into CO_2 huff-n-puff mechanisms from laboratory experiment and single-well pilot test in the Lucaogou tight oil reservoir, Jimsar sag, China. Geoenergy Sci. Eng. 232, 212456. https://doi.org/10.1016/j.geoen.2023.212456.

Song, S., Chang, J., Guan, Q., Song, Z., Wan, Y., Zhang, K., Xu, J., Fan, Z., Zhang, Y., Wang, H., Liu, X., 2024. Characteristics of crude oil production in microscopic pores of CO_2 huff and puff in shale oil reservoirs. Energy Fuels 38 (5), 3982–3996. https://doi.org/10.1021/acs.energyfuels.3c04403.

Song, Y., Kausik, R., 2019. NMR application in unconventional shale reservoirs–A new porous media research frontier. Prog. Nucl. Magn. Reson. Spectrosc. 112, 17–33. https://doi.org/10.1016/j.pnmrs.2019.03.002.

Song, Y., Song, Z., Chen, Z., Mo, Y., Zhou, Q., Tian, S., 2024a. Simulation of CO_2 enhanced oil recovery and storage in shale oil reservoirs: Unveiling the impacts of nano-confinement and oil composition. Adv. Geo-Energy. Res. 13 (2), 106–118. https://doi.org/10.46690/ager.2024.08.05.

Song, Y., Song, Z., Meng, Y., Chen, Z., Han, X., Feng, D., 2024b. Multi-phase behavior and pore-scale flow in medium-high maturity continental shale reservoirs with Oil, CO_2, and water. Chem. Eng. J. 484, 149679. https://doi.org/10.1016/j.cej.2024.149679.

Song, Y., Song, Z., Mo, Y., Chen, F., Jing, Y., Han, X., Bai, M., Tian, S., 2025a. CO_2 injection induced thermodynamic shifts in continental and marine shale oils. Energy 328, 136535. https://doi.org/10.1016/j.energy.2025.136535.

Song, Y., Song, Z., Mo, Y., Zhou, Q., Jing, Y., Chen, F., Tian, S., Chen, Z., 2025b. Determination of minimum miscibility and near-miscibility pressures for CO_2-oil mixtures in shale reservoirs. Fuel 388, 134531. https://doi.org/10.1016/j.fuel.2025.134531.

Song, Y., Song, Z., Zhang, Y., Xie, Z., Zhang, L., Wang, D., Hui, G., 2022. Pore scale performance evaluation and impact factors in nitrogen huff-n-puff EOR for tight oil. Pet. Sci. 19 (6), 2932–2940. https://doi.org/10.1016/j.petsci.2022.05.012.

Song, Z., Li, J., Sun, L., Huo, X., Zhou, Z., Xiao, D., Shen, A., Liu, J., 2024. Control of physical properties by the matching between rock components and pore structure in shale reservoirs of the Permian lucaogou Formation, Jimusar Sag. Energy Fuels 38 (14), 12938–12948. https://doi.org/10.1021/acs.energyfuels.4c02012.

Tan, Y., Zhang, Y., Xiong, H., Tian, S., Wang, F., 2024. Molecular dynamics of CO_2 stripping oil on quartz surfaces. Processes 12 (12), 2776. https://doi.org/10.3390/pr12122776.

Wang, F., Wang, L., 2022. Pore structure analysis and permeability prediction of shale oil reservoirs with HPMI and NMR: A case study of the Permian Lucaogou Formation in the Jimsar Sag, Junggar Basin, NW China. J. Petrol. Sci. Eng. 214, 110503. https://doi.org/10.1016/j.petrol.2022.110503.

Wang, J., Zhang, P., Lu, S., Lin, Z., Li, W., Zhang, J., Gao, W., Zhou, N., Chen, G., Yin, Y., Wu, H., 2025. Insights into microscopic oil occurrence characteristics in shales from the Paleogene Funing Formation in Subei Basin, China. Pet. Sci. 22 (1), 55–75. https://doi.org/10.1016/j.petsci.2024.07.025.

Wang, J., Zhou, L., Jin, J., Liu, J., Chen, J., Jiang, H., Zhang, B., 2021. Pore structure, hydrocarbon occurrence and their relationship with shale oil production in Lucaogou Formation of Jimsar Sag, Junggar Basin. Petrol. Geol. Exp. 43 (6), 941–948. (in Chinese).

Wang, Y., Cao, R., Jia, Z., Wang, B., Ma, M., Cheng, L., 2024. A multi-mechanism numerical simulation model for CO_2-EOR and storage in fractured shale oil reservoirs. Pet. Sci. 21 (3), 1814–1828. https://doi.org/10.1016/j.petsci.2024.02.006.

Wang, Y., Pu, J., Wang, L., Wang, J., Jiang, Z., Song, Y., Wang, C., Wang, Y., Jin, C., 2016. Characterization of typical 3D pore networks of Jiulaodong formation shale using nano-transmission X-ray microscopy. Fuel 170, 84–91. https://doi.org/10.1016/j.fuel.2015.11.086.

Wang, Y., Sun, S., 2021. Multiscale pore structure characterization based on SEM images. Fuel 289, 119915. https://doi.org/10.1016/j.fuel.2020.119915.

Xiao, Q., Yang, Z., Wang, Z., Qi, Z., Wang, X., Xiong, S., 2020. A full-scale characterization method and application for pore-throat radius distribution in tight oil reservoirs. J. Petrol. Sci. Eng. 187, 106857. https://doi.org/10.1016/j.petrol.2019.106857.

Xie, J., Cui, X., Li, W., Zhu, J., Wu, X., Chu, Y., Chen, Y., Tang, T., Zhu, S., Wu, C., Zhang, J., 2022. Exploration and practice of benefit development of shale oil in Jimsar Sag, Junggar Basin. China Petrol. Exp. 27 (1), 99–110. https://doi.org/10.3969/j.issn.1672-7703.2022.01.009.

Yao, Y., Liu, D., Che, Y., Tang, D., Tang, S., Huang, W., 2010. Petrophysical characterization of coals by low-field nuclear magnetic resonance (NMR). Fuel 89 (7), 1371–1380. https://doi.org/10.1016/j.fuel.2009.11.005.

Zhang, P., Lu, S., Li, J., Chang, X., Zhang, J., Pang, Y., Lin, Z., Chen, G., Yin, Y., Liu, Y.Q., 2023. Quantitative characterization of shale pore connectivity and controlling factors using spontaneous imbibition combined with nuclear magnetic resonance T_2 and T_1-T_2. Pet. Sci. 20 (4), 1947–1960. https://doi.org/10.1016/j.petsci.2023.03.011.

Zhang, Y., Song, Z., Meng, Y., Zhang, L., Zhou, Q., 2023. Characterization of micro-nano pore structures in shale oil reservoirs and FIB-SEM 3D reconstruction: A case study. In: SPE/IATMI Asia Pacific Oil & Gas Conference and Exhibition. https://doi.org/10.2118/215301-MS.

Zhou, Y., Zhong, X., Nie, X., 2024. Identification and parameter characterization of pores and fractures in shales based on multi-scale digital core data. Adv. Geo-Energy Res. 13 (2), 146–160. https://doi.org/10.46690/ager.2024.08.08.

Zhu, J., Wang, F., Wang, J., Li, Z., Zhang, S., 2025. Investigation on energy enhancement of shale oil imbibition under different fracture fluid injection Methods—A case investigation of Jimsar Lucaogou Formation. Energies 18 (6), 1412. https://doi.org/10.3390/en18061412.